Acoustic Landau levels in a synthetic magnetic field with a symmetric gauge

Pan Li[1,2,‡] Wencan Chen,[1,‡] Jiaxin Chen,[1] Wei Luo,[1,*] and Degang Zhao[2,†]

[1]*School of Integrated Circuits, Huazhong University of Science and Technology, Wuhan 430074, China*
[2]*Department of Physics, Huazhong University of Science and Technology, Wuhan 430074, China*

Pseudomagnetic fields are promising for manipulating classical waves, including optic, acoustic, and elastic waves. One fascinating phenomenon is the presence of Landau energy levels and the involved quantum Hall effect, which are usually considered to exist only in quantum systems. Unlike using synthetic Landau gauge fields, as in existing works, here we successfully create a symmetric gauge field to achieve a large-area uniform pseudomagnetic field in a two-dimensional phononic crystal by introducing linear variations in the single-cell parameters of the scatterer along both the x and y directions. Discrete Landau levels are generated near the Dirac cone region, and the unidirectional propagation of acoustic waves along the domain wall, i.e., quantum Hall transport, is observed in experiment. The proposed structure offers greater flexibility by allowing free choice of the effective vector potential. Our study expands the application perspective of artificial acoustic devices that rely on a pseudomagnetic field.

I. INTRODUCTION

Landau quantization, named after physicist Lev Landau, elucidates the quantization of the cyclotron orbits of charged particles in a uniform magnetic field, yielding discrete energy levels known as Landau levels [1]. These levels influence electronic susceptibility in metals, seen as Landau diamagnetism. They are pivotal in understanding phenomena like the de Haas–van Alphen and Shubnikov–de Haas effects, essential for the integer quantum Hall effect in strong magnetic fields. However, observing analogous phenomena in magnetic fields with neutral particles is elusive due to their inability to couple with electromagnetic gauge potentials directly. Nonetheless, inventive designs of acoustic artificial structures have facilitated the creation of pseudomagnetic fields (PMFs), leading to distinct magnetic effects in classic acoustic waves. In the 1990s, a vorticity filament mimicked a magnetic field in a solenoid, inducing the Aharonov-Bohm effect in an acoustic wave [2–4]. Then, the acoustic Zeeman effect and nonreciprocal propagation were realized by introducing circulating airflow as static bias in a three-port circulator structure [5]. Following this, effective magnetic fields induced by circulating flows were integrated into periodic phononic crystals (PCs), resulting in the observation of the acoustic quantum Hall effect and topological edge states [6–11].

Recently, it was demonstrated that a giant PMF can be produced in strained graphene flakes. The dynamical behavior of electrons in the strained graphene is identical to that of those in a realistic magnetic field [12–20]. More recently, this ingenious design was transplanted into artificial optical and acoustic structures. Intriguingly, neutral photons and phonons can also exhibit magnetic effects, such as quantized Landau levels induced by synthetic uniform PMFs [21–29]. However, the imposed well-designed strain on the structure is not easy to implement and control over a large area in experiments. To overcome this, another easier scheme has been proposed [30–34]. Researchers first constructed a two-dimensional (2D) acoustic graphenelike honeycomb lattice to produce Dirac points at the Brillouin zone corners, which mimic the spin-1/2 massless Dirac fermions. After that, they introduced a deformation on the scatterers, and the Dirac points were found to shift along the $\Gamma - K$ direction in momentum space. The momentum variation $\delta\mathbf{k}$ is proportional to a vector potential with Landau gauge $\mathbf{A} = (-By, 0, 0)$ and then a perpendicular uniform PMF $\mathbf{B} = \nabla \times \mathbf{A} = (0, 0, B)$ is produced. In this gauge field, the flat Landau levels emerge in the energy spectrum and the corresponding acoustic quantum Hall effect is demonstrated. For a given magnetic field, the vector potential is not unique, because curl-free components can be added without changing the observed magnetic field, i.e., $\mathbf{A} \rightarrow \mathbf{A} + \nabla\phi$. This is well known as gauge invariance and it offers a degree of freedom in choosing $\mathbf{A}$. For a uniform and constant magnetic field, two commonly used gauges are the Landau gauge and the symmetric gauge [35,36].

---

*Contact author: luowei@hust.edu.cn
†Contact author: dgzhao@hust.edu.cn
‡These authors contributed equally to this work.

These have identical energy spectra but distinct eigenfunctions. The Landau gauge naturally leads to Hermite-type eigenfunctions, which respect translational symmetry along the x or y direction, while the symmetric gauge leads to Laguerre-type eigenfunctions, which respect rotational symmetry around the coordinate origin [37,38]. In this work, we create a synthetic large-area symmetric gauge $\mathbf{A} = (-By/2, Bx/2, 0)$ in a PC. The acoustic Landau levels and the relevant quantum Hall-like edge states are demonstrated by both theory and experiment. We also reveal the different field distributions and propagation characteristics in the symmetric gauge.

II. RESULTS

A. Theory and Landau levels

We begin by considering a 2D PC that is composed of a triangular array of solid elliptical cylinders in an air background. The semimajor and semiminor axes of the elliptic cross section of the cylinder are r_1 and r_2, respectively. The lattice constant $a = 25$ mm. θ is the intersection angle between r_1 and the x axis, denoting the orientation degree of freedom of the scatterers. The unit cell is schematically sketched in Fig. 1(a). Here we define the flattening of the ellipse as $\xi = (r_1 - r_2)/r_2$, and the filling ratio $2\pi r_1 r_2/\sqrt{3}a^2$ is kept at 0.37 for simplicity. Firstly when $\xi = 0$, the scatterers are circular columns and the lattice

hosts Dirac cones at the Brillouin zone corners K and K'. As ξ becomes nonzero, i.e., the scatterer becomes an elliptical cylinder but θ remains zero, the Dirac cones shift along the x direction in momentum space and the magnitude of the k shift is proportional to ξ. Accordingly, a synthetic Landau gauge is produced [30]. On this basis, we rotate the elliptical cylinder around its center, i.e., $\theta \neq 0°$. Fortunately, the Dirac cone still survives and rotates around the K point in the 2D momentum space. The deformation and rotation of scatterers, as well as the induced PMF, do not break time-reversal symmetry. Then the Dirac cone near the K' point shifts along the opposite direction to that near the K point. For brevity, hereafter we focus only on the physics near the K point, and that of the K' point can be obtained by applying a time-reversal operation. The evolution of the Dirac cone can be found in Sec. A of the Supplemental Material [39]. The survival of the Dirac cone is guaranteed by the symmetric properties of the lattice [40–43]. When the rotation angle θ of the elliptical scatterer changes from $0°$ to $180°$, the Dirac cone also completes a revolution and the trajectory of the Dirac point forms an enclosed curve, as is shown in Fig. 1(b). With the Dirac point shifting to $\delta\mathbf{k} = (\delta k_x, \delta k_y)$, the effective Dirac Hamiltonian can be written as follows [31–33]:

$$\hat{H}_{\text{eff}} = v_D[(k_x - \delta k_x)\sigma_x + (k_y - \delta k_y)\sigma_y]. \quad (1)$$
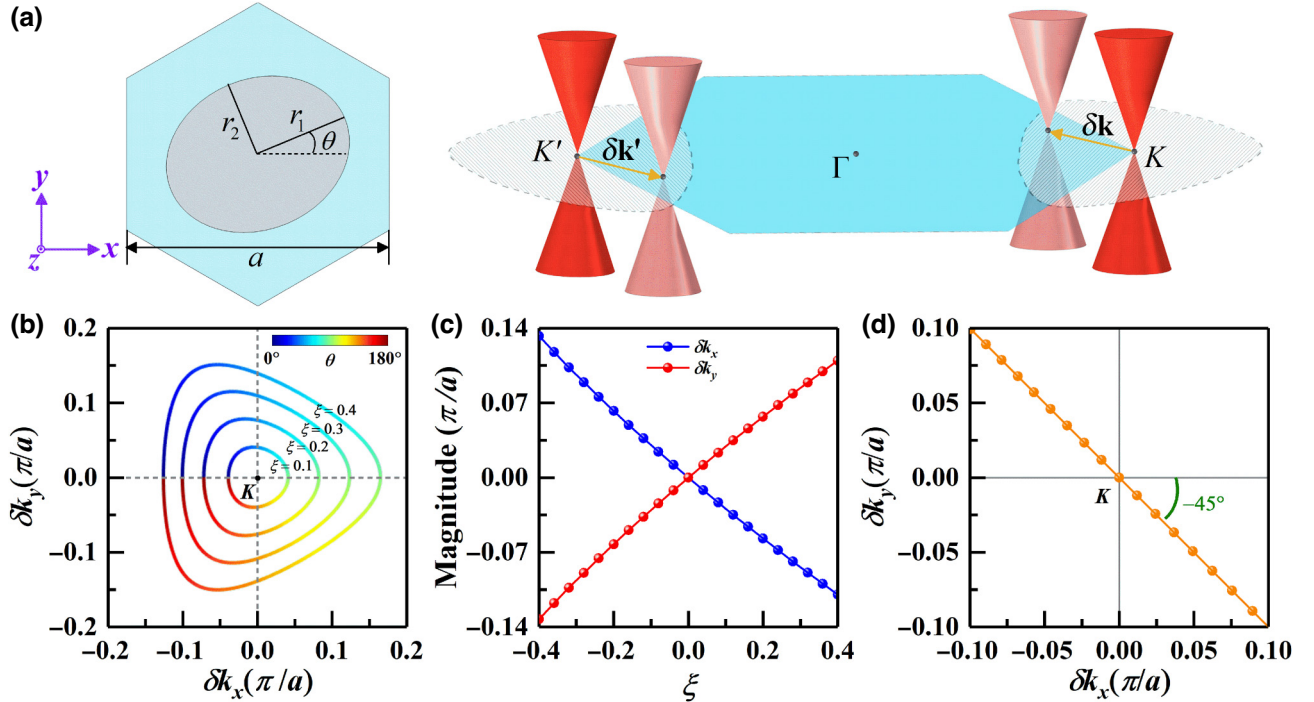

FIG. 1. The movement of Dirac points in the Brillouin zone. (a) The unit cell of a triangular lattice phononic crystal with an elliptical scatterer (left) and the shift of the Dirac points in the Brillouin zone (right). (b) Contours of the position of Dirac points in the momentum space around the K point with different deformation degrees ξ as the rotation angle θ of the elliptical scatterer changes from $0°$ to $180°$. (c) The magnitude of the spatial shift of Dirac point versus the deformation degree ξ as the elliptical scatterer rotates by $\theta = 22.5°$; (d) the trajectory of Dirac point for the case in (c).

Here v_D is the Dirac velocity, and σ_x, σ_y are Pauli matrices. The spatial shift of the Dirac point implies a vector potential $\mathbf{A} = \delta\mathbf{k}$ enters the Hamiltonian. Our proposed structure renders a free choice of the vector potential, not just the Landau gauge as in previous works [31–33]. Without losing generality, we set $\theta = 22.5°$. As is shown in Fig. 1(c), the momentum shifts in the x and y directions have the same magnitude but different signs. Both exhibit linear dependence on ξ, and the numerical fitting linear relations are $\delta k_x = -c\xi$, $\delta k_y = c\xi$, where the slope $c = 0.3\pi/a$ depends on the filling ratio. More details can be seen in Sec. A of the Supplemental Material [39]. Thus, the Dirac point shifts along the line $k_x + k_y = 0$, as shown in Fig. 1(d). On these grounds, with the linear variation of ξ along both x and y directions such that $\xi(x) = Bx/2c$, $\xi(y) = By/2c$, a typical symmetric gauge field $A_x(y) = -c\xi(y) = -By/2$, $A_y(x) = c\xi(x) = Bx/2$ can be easily constructed. Consequently, a uniform constant PMF $\nabla \times \mathbf{A} = B\hat{z}$ perpendicular to the x-y plane can be obtained. This constant PMF causes the linear Dirac cone to split into a sequence of discrete quantized Landau levels [44–54].

B. Simulation of the acoustic quantum Hall effect

To verify theoretical prediction, we construct a 150×173-layer PC with linearly decreasing ξ along both x and y directions with $\theta = 22.5°$, as shown in Fig. 2(a). The variation interval of ξ is $[-0.5, 0.5]$ and the corresponding PMF is $B = -0.0063a^{-2}$ (more details about structural design can be found in Sec. B of the Supplemental Material [39]). We present 300 calculated eigenvalues near the Dirac region for the PC in ascending order of the number of states in Fig. 2(b). This clearly shows discrete plateaus in the energy spectrum, which is the hallmark of the emergence of Landau levels. The centered plateau

with the Dirac frequency $f_D = 7225$ Hz is the zeroth-order Landau level. The energy gaps between the Landau levels satisfy $\Delta f_n = \text{sign}(n)\sqrt{|n|}\omega_c/2\pi$ measured with respect to f_D, where the integer n is the order of the Landau level and $\omega_c = v_D\sqrt{2|B|}$ is known as the acoustic analogue of the cyclotron frequency [31,32]. The numerical ω_c calculated by the dispersion relation is 902 Hz, which agrees well with the numerical result of 910 Hz obtained through the data in Fig. 2(b). The energy gaps between the Landau levels increase proportionally with $\sqrt{|Bn|}$, which is consistent with the behavior of Dirac fermions in a high-intensity magnetic field [29].

The most fascinating property of the PMF system is the propagation of quantum Hall edge states in the gaps between two neighboring Landau levels. To demonstrate this, we design a 150×173-layer PC (all the structural parameters are identical to those in Fig. 2) to investigate the propagation patterns of acoustic waves. In Fig. 3(a), a point source is placed at the bottom-left corner of the PC. For the state S_1 at frequency 7150 Hz between the zeroth and -1st Landau levels, the acoustic wave propagates along the left and top boundaries in sequence and finally reaches the upper-right corner. For the state S_3 at frequency 7300 Hz between the zeroth and $+1$st Landau levels, the acoustic wave chooses the bottom and right boundaries as the propagating path, which can be regarded as a time-reversal operation to state S_1. By contrast, for the extended state S_2 at the zeroth Landau level (frequency 7225 Hz), the sound energy spreads into the bulk. Owing to the preservation of time-reversal symmetry, when a point source is located at the top-left or top-right corner, the edge state S_1 invariably propagates along the left and top boundaries. Similarly, when the point source is positioned at the bottom-right or top-right corner, the edge state S_3 always propagates along the bottom and right boundaries.
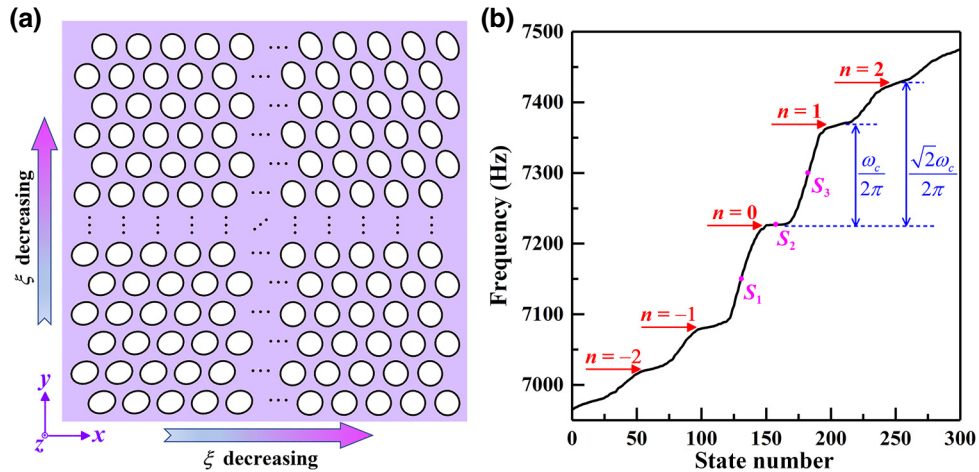

FIG. 2. Symmetric gauge field model. (a) Supercell model with ξ decreasing in both x and y directions as the elliptical scatterers rotate by $\theta = 22.5°$; (b) Landau levels near the Dirac point in a 150×173-layer supercell model, where n represents the order of the Landau level and ω_c is the acoustic analogue of the cyclotron frequency.
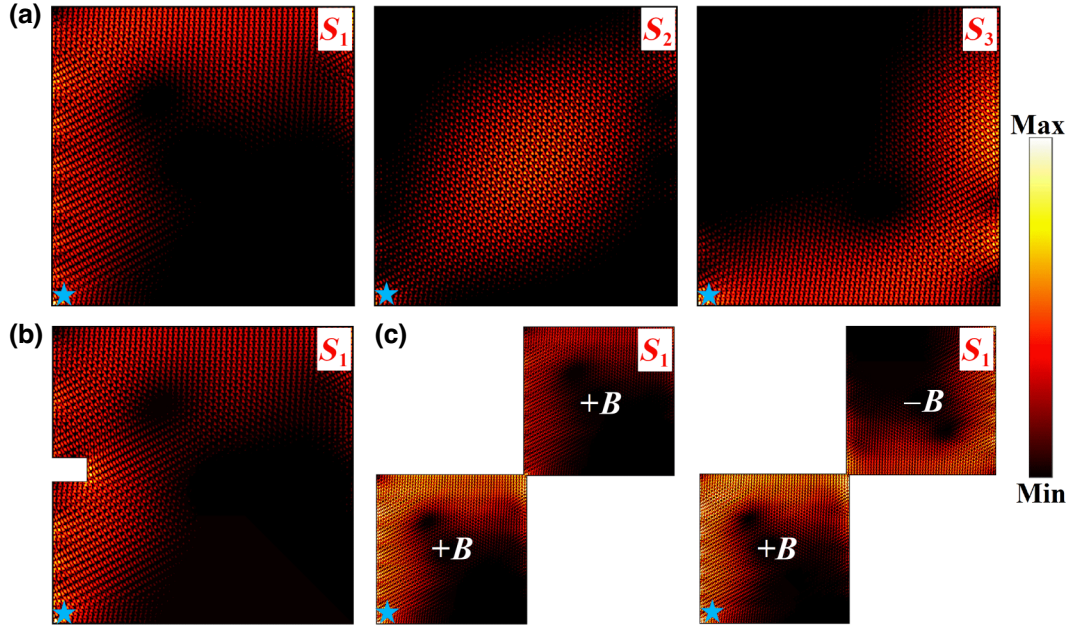
FIG. 3.   Simulation of acoustic quantum Hall effect induced by the pseudomagnetic field (PMF). (a) The sound field distributions at three different frequencies, corresponding to the states marked as S_1, S_2, and S_3 in Fig. 2(b). (b) The robustness of the propagation of an acoustic quantum Hall edge state against the defect in the propagation path. (c) The propagation of an acoustic quantum Hall edge state in two corner-connected PMF domains. The point sources, represented by the light blue stars, are located at the bottom-left corner in all parts.

See Fig. S3 in Sec. C of the Supplemental Material [39] for more details. This asymmetrical edge response stems from the differing structural details of the top-left and bottom-right edges of the sample [31].

One outstanding property of the quantum Hall edge states in the PMF system is the robustness against defects. To illustrate this, we introduce a rectangular defect on the left side. As shown in Fig. 3(b), the acoustic wave for state S_1 still propagates along the left and top boundaries in sequence and finally reaches the upper-right corner. Further, we introduce square and trapezoidal defects in the top-left corner and on the upper side (see Fig. S4 in Sec. D of the Supplemental Material [39]), respectively, and the propagation of the edge states keeps the original path. This intuitively reveals the immunity of acoustic quantum Hall edge states to defects, regardless of the shape and location of the defect.

In our design, the direction of PMF can be effortlessly obtained by rotating the supercell by 180° without any change of energy spectrum. By diagonally combining any two supercells with identical PMF or opposing PMF, it is possible to selectively control the propagation direction of sound quantum Hall edge states. As an example, we consider two corner-connected identical 80×92-layer supercells, with the deformation of elliptical scatterers gradually decreasing along both the x and y axes, resulting in a PMF of magnitude $B = -0.0048a^{-2}$ oriented along the positive z axis. Firstly, a point source with a frequency

of 7150 Hz (state S_1) is positioned at the bottom-left corner of the merged supercells, as shown in the left panel of Fig. 3(c). Thus, the sound wave propagates along the left boundary and upper boundary of the first supercell, couples to the second supercell at the upper right corner, and continues propagating along the left boundary and upper boundary of the second supercell. Conversely, we rotate the second supercell to form a $(+B, -B)$ PMF distribution. Consequently, the propagation route in the first supercell remains unchanged, while the acoustic wave propagates along the bottom boundary and right boundary in the second supercell. Through this approach, we achieve precise control over the direction of sound wave propagation by intentionally designing the supercell structure and source frequencies, providing a novel way to modulate the propagation of quantum Hall edge states.

C. Experimental measurement of acoustic quantum Hall edge states

Theoretically, as the number of cells or the PMF strength B increases, the number of degenerate states increases, and the state of the Landau level becomes flatter, thus higher degeneracy is achieved [29], resulting in better localization of edge states (see Figs. S5 and S6 in Sec. E of the Supplemental Material [39]). However, the inevitable enormous dissipation in large-size structures should be considered in the experiment. Hence, we experimentally design a

40×40-layer supercell to replicate PMF-induced acoustic quantum Hall edge states. Utilizing 3D printing technology associated with a nominal fabrication error of about 0.02 cm, we craft a sample (of size 1000×866 mm^2) containing 1600 photosensitive elliptical resin scatterers fixed on a substrate, as depicted in Fig. 4(a). Here, the filling ratio of the lattice remains 0.37, and the oriented angle of all elliptical scatterers is 22.5°. Linear deformations are introduced along both the x and y directions to produce a constant PMF $B = -0.0041a^{-2}$. For accurate sound field distribution detection, while minimizing sound wave dispersion, a transparent plastic cover is placed atop the model. Solid steel plates are stuck around the sample to play the role of rigid boundaries. In experiments,

one loudspeaker is placed in a selected hole at the bottom-left corner of the sample and driven by the multifunctional signal generator (Tektronix AFG3022C). Sound intensities are measured by inserting a microphone (1/8-in. Brüel & Kjær 4138-A-015) into the perforated holes. All the data are recorded by a Brüel & Kjær 3160-A-042 four-channel analyzer. The sampling time of data is set to 3 s in the measurement. The frequency response is obtained with the fast Fourier transform analysis of Brüel & Kjær PULSE software LABSHOP.

To demonstrate the propagation of the acoustic quantum Hall edge states, two detectors are placed at the upper-left corner (detector 1) and bottom-right corner (detector 2), respectively, to perform comparative
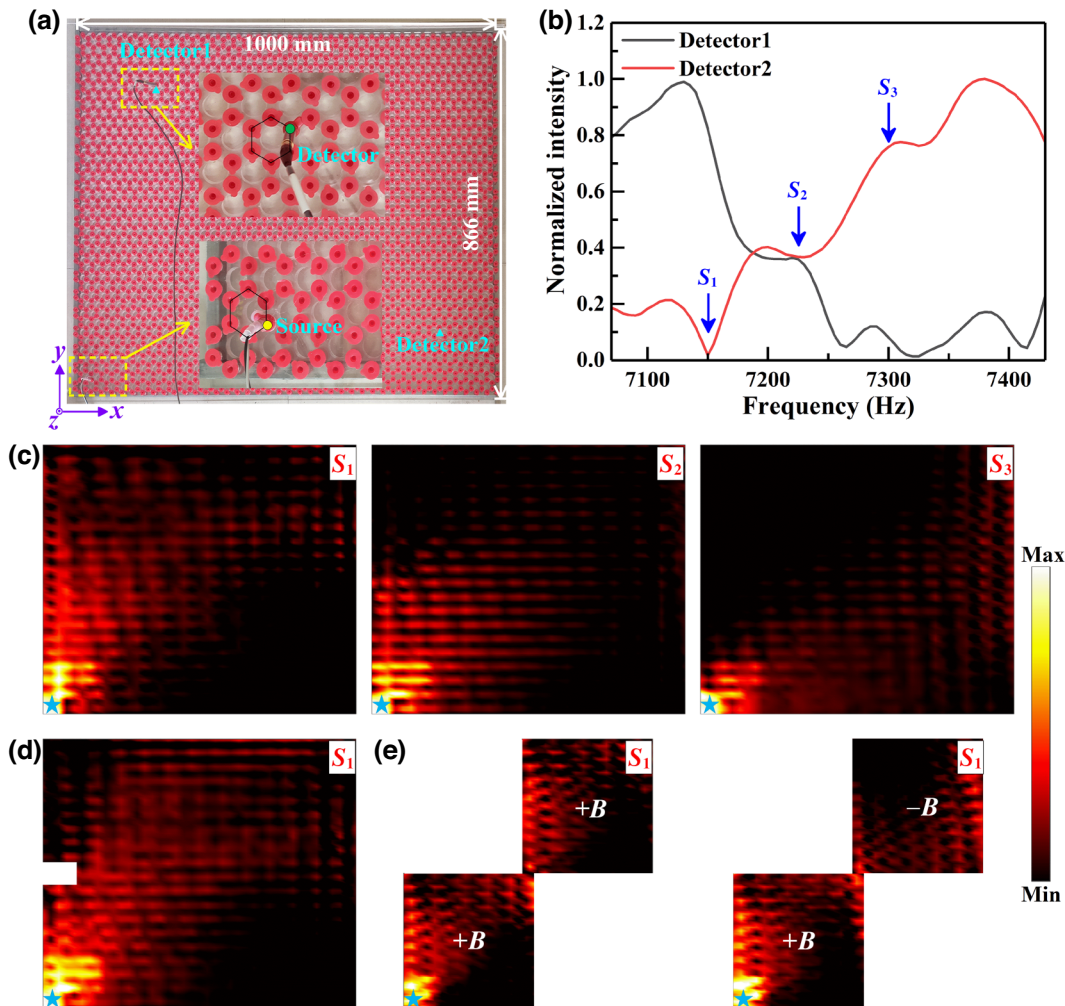

FIG. 4. Experimental measurement of acoustic quantum Hall edge states. (a) Experimental setup of a 40×40-layer supercell sample, with a pseudomagnetic field (PMF) of $B = -0.0041a^{-2}$. The insets are magnified images of the setup of the sound source and the detector. (b) Experimental measurement of acoustic field intensity with the sound source located at the bottom-left corner, with detector 1 located near the upper-left corner and detector 2 located near the bottom-right corner. Full space experimental measurement of acoustic field distributions for three cases: (c) propagation of three states S_1, S_2, and S_3 marked in Fig. 2(b) in one single supercell; (d) robustness of the acoustic quantum Hall edge state against the defect for the state S_1; (e) propagation of acoustic quantum Hall edge state in two corner-connected PMF domains for the state S_1. The frequencies corresponding to states S_1, S_2, and S_3 are 7150, 7225, and 7300 Hz, respectively.

measurements. Figure 4(b) presents the measured frequency spectra of sound wave intensity. Around the frequency 7225 Hz, both detectors exhibit nearly equivalent sound field strength, which demonstrates the bulk states associated with the zeroth Landau level. As the source frequency decreases to the gap between the -1st and zeroth Landau levels, the sound field strength at detector 1 experiences a notable increase, while that at detector 2 undergoes a significant decrease. This implies the sound waves choose to propagate along the upper-left route. In contrast, as the wave frequency increases to the gap between $+1$st and zeroth Landau levels, the detected intensity at detector 2 increases while that at detector 1 decreases, which indicates the sound waves change the propagating route to the bottom-right.

To further validate the existence of PMF-induced acoustic quantum Hall topological edge states, we conduct full space measurements of the acoustic field distribution for three states marked in Fig. 4(b), as shown in Fig. 4(c). For the state S_1 between the zeroth and -1st Landau levels, the sound wave initially propagates along the left boundary until it reaches the upper-left corner, and sequentially turns to the upper boundary to eventually arrive at the upper-right corner. For the bulk state S_2 at the zeroth Landau level, the sound wave spreads into the whole sample. Meanwhile, for the state S_3 between the zeroth and $+1$st Landau levels, the sound wave flips to another propagation route: bottom boundary, bottom-right corner, right boundary, upper-right corner. The experimental results closely align with the simulation results presented in Fig. 3(a).

Furthermore, we validate the robustness of the PMF-induced acoustic quantum Hall edge states against defects. To illustrate this, we introduce a rectangular defect $(100 \times 69 \text{ mm}^2)$ on the left side, as shown in Fig. 4(d). The one-way propagation of sound waves for the state S_1 is not affected by the scattering of the defect, which agrees well with the simulation result Fig. 3(b).

Additionally, we conduct further experiments to verify the selective propagation route of acoustic quantum Hall edge states in two corner-connected supercells. The left panel of Fig. 4(e) illustrates that when two supercells with the same PMF $(+B, +B)$ are combined, the sound wave for state S_1 propagates along the left-to-upper route in both two supercells. However, when the second supercell is rotated by $180°$ to obtain a PMF of $-B$, the sound wave in the first supercell maintains the original propagation route, while when coupled into the second supercell, the propagation route flips to the bottom-to-right route, due to the flipping of the PMF direction. The experimental results also agree quite well with the simulation result shown in Fig. 3(c). In summary, our experimental findings unequivocally demonstrate that in the gap between two neighboring Landau levels, sound waves exhibit robust propagation along boundaries with distinct routes, which can be conveniently tuned by the flipping of the direction of the PMF.

This provides direct evidence for PMF-induced acoustic quantum Hall topological edge states and holds significant importance for comprehending and harnessing topological phenomena in sound waves.

III. CONCLUSION

In conclusion, we have achieved the generation of Landau levels in a 2D phononic crystal by introducing symmetric gauge fields through linear variations in single-cell parameters along both the x and y directions, representing a significant advancement in the field of acoustic wave manipulation. The unidirectional propagation of acoustic waves along domain walls, akin to quantum Hall transport, further verifies the effectiveness of our proposed approach. The experimental observation reinforces the potential practical applications of our findings in the development of novel acoustic devices and technologies. Since the trajectory of the Dirac point in our lattice forms a closed curve in momentum space, the effective vector potential can have any orientation. Thus, our design provides great flexibility for choosing the effective vector potential and PMF. For example, apart from the most frequently used Landau gauge and symmetric gauge, we can also construct an atypical gauge field to generate a constant perpendicular PMF (see Sec. F of the Supplemental Material [39]), and even an inhomogeneous PMF [55,56]. The extreme degrees of freedom to construct synthetic PMFs will greatly expand the versatility and adaptability of wave manipulation in PCs. The success of our work not only opens alternative doors for controlling classical waves such as acoustic and elastic waves, but also bridges the gap between classical and quantum phenomena in wave systems. The excitation of acoustic quantum Hall edge states and the free control of the propagation route have potential application value in designing acoustic wave modulation devices.

ACKNOWLEDGMENTS

---

[1] L. Landau, Diamagnetismus der Metalle, Z. Phys. **64,** 629 (1930).

[2] P. Roux, J. de Rosny, M. Tanter, and M. Fink, The Aharonov-Bohm effect revisited by an acoustic time-reversal mirror, Phys. Rev. Lett. **79,** 3170 (1997).

[3] F. Vivanco, F. Melo, C. Coste, and F. Lund, Surface wave scattering by a vertical vortex and the symmetry of the Aharonov-Bohm wave function, Phys. Rev. Lett. **83,** 1966 (1999).

[4] C. Coste, F. Lund, and M. Umeki, Scattering of dislocated wavefronts by vertical vorticity and the Aharonov-Bohm effect. I. Shallow water, Phys. Rev. E **60,** 4908 (1999).

[5] R. Fleury, D. L. Sounas, C. F. Sieck, M. R. Haberman, and A. Alù, Sound isolation and giant linear nonreciprocity in a compact acoustic circulator, Science **343,** 516 (2014).

[6] Z. Yang, F. Gao, X. Shi, X. Lin, Z. Gao, Y. Chong, and B. Zhang, Topological acoustics, Phys. Rev. Lett. **114,** 114301 (2015).

[7] A. B. Khanikaev, R. Fleury, S. H. Mousavi, and A. Alù, Topologically robust sound propagation in an angular-momentum-biased graphene-like resonator lattice, Nat. Commun. **6,** 8260 (2015).

[8] X. Ni, C. He, X.-C. Sun, X.-p. Liu, M.-H. Lu, L. Feng, and Y.-F. Chen, Topologically protected one-way edge mode in networks of acoustic resonators with circulating air flow, New J. Phys. **17,** 053016 (2015).

[9] Z.-G. Chen and Y. Wu, Tunable topological phononic crystals, Phys. Rev. Appl. **5,** 054021 (2016).

[10] Y. Ding, Y. Peng, Y. Zhu, X. Fan, J. Yang, B. Liang, X. Zhu, X. Wan, and J. Cheng, Experimental demonstration of acoustic Chern insulators, Phys. Rev. Lett. **122,** 014302 (2019).

[11] D. Zhao, Y.-T. Wang, K.-H. Fung, Z.-Q. Zhang, and C. T. Chan, Acoustic metamaterials with spinning components, Phys. Rev. B **101,** 054107 (2020).

[12] Y. Zhang, Y.-W. Tan, H. L. Stormer, and P. Kim, Experimental observation of the quantum Hall effect and Berry's phase in graphene, Nature **438,** 201 (2005).

[13] F. Guinea, M. I. Katsnelson, and A. K. Geim, Energy gaps and a zero-field quantum Hall effect in graphene by strain engineering, Nat. Phys. **6,** 30 (2010).

[14] N. Levy, S. A. Burke, K. L. Meaker, M. Panlasigui, A. Zettl, F. Guinea, A. H. C. Neto, and M. F. Crommie, Strain-induced pseudo–magnetic fields greater than 300 tesla in graphene nanobubbles, Science **329,** 544 (2010).

[15] T. Low and F. Guinea, Strain-induced pseudomagnetic field for novel graphene electronics, Nano Lett. **10,** 3551 (2010).

[16] F. Guinea, A. K. Geim, M. I. Katsnelson, and K. S. Novoselov, Generating quantizing pseudomagnetic fields by bending graphene ribbons, Phys. Rev. B **81,** 035408 (2010).

[17] K. K. Gomes, W. Mar, W. Ko, F. Guinea, and H. C. Manoharan, Designer Dirac fermions and topological phases in molecular graphene, Nature **483,** 306 (2012).

[18] B.-L. Wu, Q. Wei, Z.-Q. Zhang, and H. Jiang, Transport property of inhomogeneous strained graphene, Chin. Phys. B **30,** 030504 (2021).

[19] P. Nigge, A. C. Qu, É Lantagne-Hurtubise, E. Mårsell, S. Link, G. Tom, M. Zonno, M. Michiardi, M. Schneider, S. Zhdanovich, G. Levy, U. Starke, C. Gutiérrez, D. Bonn, S. A. Burke, M. Franz, and A. Damascelli, Room temperature strain-induced Landau levels in graphene on a wafer-scale platform, Sci. Adv. **5,** eaaw5593 (2019).

[20] C.-C. Hsu, M. L. Teague, J.-Q. Wang, and N.-C. Yeh, Nanoscale strain engineering of giant pseudo-magnetic fields, valley polarization, and topological channels in graphene, Sci. Adv. **6,** eaat9488 (2020).

[21] M. C. Rechtsman, J. M. Zeuner, A. Tünnermann, S. Nolte, M. Segev, and A. Szameit, Strain-induced pseudomagnetic field and photonic Landau levels in dielectric structures, Nat. Photonics **7,** 153 (2013).

[22] H. Schomerus and N. Y. Halpern, Parity anomaly and Landau-level lasing in strained photonic honeycomb lattices, Phys. Rev. Lett. **110,** 013903 (2013).

[23] H. Abbaszadeh, A. Souslov, J. Paulose, H. Schomerus, and V. Vitelli, Sonic Landau levels and synthetic gauge fields in mechanical metamaterials, Phys. Rev. Lett. **119,** 195502 (2017).

[24] O. Jamadi, E. Rozas, G. Salerno, M. Milićević, T. Ozawa, I. Sagnes, A. Lemaître, L. Le Gratiet, A. Harouri, I. Carusotto, J. Bloch, and A. Amo, Direct observation of photonic Landau levels and helical edge states in strained honeycomb lattices, Light: Sci. Appl. **9,** 144 (2020).

[25] W. Wang, W. Gao, X. Chen, F. Shi, G. Li, J. Dong, Y. Xiang, and S. Zhang, Moire fringe induced gauge field in photonics, Phys. Rev. Lett. **125,** 203901 (2020).

[26] M. Bellec, C. Poli, U. Kuhl, F. Mortessagne, and H. Schomerus, Observation of supersymmetric pseudo-Landau levels in strained microwave graphene, Light: Sci. Appl. **9,** 146 (2020).

[27] J. Guglielmon, M. C. Rechtsman, and M. I. Weinstein, Landau levels in strained two-dimensional photonic crystals, Phys. Rev. A **103,** 013505 (2021).

[28] M. Jamotte, N. Goldman, and M. Di Liberto, Strain and pseudo-magnetic fields in optical lattices from density-assisted tunneling, Commun. Phys. **5,** 30 (2022).

[29] Z. Yang, F. Gao, Y. Yang, and B. Zhang, Strain-induced gauge field and Landau levels in acoustic structures, Phys. Rev. Lett. **118,** 194301 (2017).

[30] C. Brendel, V. Peano, O. J. Painter, and F. Marquardt, Pseudomagnetic fields for sound at the nanoscale, Proc. Natl. Acad. Sci. U. S. A. **114,** E3390 (2017).

[31] X. Wen, C. Qiu, Y. Qi, L. Ye, M. Ke, F. Zhang, and Z. Liu, Acoustic Landau quantization and quantum-Hall-like edge states, Nat. Phys. **15,** 352 (2019).

[32] J.-C. Luo, L.-Y. Feng, H.-B. Huang, and J.-J. Chen, Pseudomagnetic fields and Landau levels for out-of-plane elastic waves in gradient snowflake-shaped crystals, Phys. Lett. A **383,** 125974 (2019).

[33] M. Yan, W. Deng, X. Huang, Y. Wu, Y. Yang, J. Lu, F. Li, and Z. Liu, Pseudomagnetic fields enabled manipulation of on-chip elastic waves, Phys. Rev. Lett. **127,** 136401 (2021).

[34] B. Zhang, Audible Landau levels, Nat. Phys. **15,** 307 (2019).

[35] O. Ciftja, Detailed solution of the problem of Landau states in a symmetric gauge, Eur. J. Phys. **41,** 035404 (2020).

[36] W. Zimmermann, Jr., A wave-packet description of the motion of a charged particle in a uniform magnetic field, Jr., Am. J. Phys. **57,** 593 (1989).

[37] A. Bhuiyan and F. Marsiglio, Landau levels, edge states, and gauge choice in 2D quantum dots, Am. J. Phys. **88** (11), 986 (2020).

[38] M. Wakamatsu and A. Hayashi, Physical symmetries and gauge choices in the Landau problem, Eur. Phys. J. A **58,** 121 (2022).

[39] See Supplemental Material http://link.aps.org/supple mental/10.1103/PhysRevApplied.22.014047 for (A) Dirac cone shift in momentum space, (B) designing the synthetic constant PMF with symmetric gauge, (C) simulated results about the transports of the edge states, (D) robust transport of the edge states, (E) localization analysis of the

edge states, and (F) Landau levels in atypical gauge, which includes Refs. [29,57].

[40] J. Lu, C. Qiu, S. Xu, Y. Ye, M. Ke, and Z. Liu, Dirac cones in two-dimensional artificial crystals for classical waves, Phys. Rev. B **89**, 134302 (2014).

[41] M. O. Goerbig, Electronic properties of graphene in a strong magnetic field, Rev. Mod. Phys. **83**, 1193 (2011).

[42] B. A. Bernevig and T. L. Hughes, *Topological Insulators and Topological Superconductors* (Princeton University Press, Princeton, New Jersey, 2013).

[43] B. Wunsch, F. Guinea, and F. Sols, Dirac-point engineering and topological phase transitions in honeycomb optical lattices, New J. Phys. **10**, 103027 (2008).

[44] G. Dresselhaus, Graphite Landau levels in the presence of trigonal warping, Phys. Rev. B **10**, 3602 (1974).

[45] A. H. Castro Neto, F. Guinea, N. M. R. Peres, K. S. Novoselov, and A. K. Geim, The electronic properties of graphene, Rev. Mod. Phys. **81**, 109 (2009).

[46] E. McCann and V. I. Fal'ko, Landau-level degeneracy and quantum Hall effect in a graphite bilayer, Phys. Rev. Lett. **96**, 086805 (2006).

[47] F. Guinea, A. H. Castro Neto, and N. M. R. Peres, Electronic states and Landau levels in graphene stacks, Phys. Rev. B **73**, 245426 (2006).

[48] S. Yuan, R. Roldán, and M. I. Katsnelson, Landau level spectrum of *ABA*- and *ABC*-stacked trilayer graphene, Phys. Rev. B **84**, 125455 (2011).

[49] F. Mireles and J. Schliemann, Energy spectrum and Landau levels in bilayer graphene with spin-orbit interaction, New J. Phys. **14**, 093026 (2012).

[50] L. Ju, L. Wang, X. Li, S. Moon, M. Ozerov, Z. Lu, T. Taniguchi, K. Watanabe, E. Mueller, F. Zhang, D. Smirnov, F. Rana, and P. L. McEuen, Unconventional valley-dependent optical selection rules and Landau level mixing in bilayer graphene, Nat. Commun. **11**, 2941 (2020).

[51] G. Li, A. Luican-Mayer, D. Abanin, L. Levitov, and E. Y. Andrei, Evolution of Landau levels into edge states in graphene, Nat. Commun. **4**, 1744 (2013).

[52] M. T. Greenaway, E. E. Vdovin, A. Mishchenko, O. Makarovsky, A. Patanè, J. R. Wallbank, Y. Cao, A. V. Kretinin, M. J. Zhu, S. V. Morozov, V. I. Fal'ko, K. S. Novoselov, A. K. Geim, T. M. Fromhold, and L. Eaves, Resonant tunneling between the chiral Landau states of twisted graphene lattices, Nat. Phys. **11**, 1057 (2015).

[53] S.-Y. Li, K.-K. Bai, L.-J. Yin, J.-B. Qiao, W.-X. Wang, and L. He, Observation of unconventional splitting of Landau levels in strained graphene, Phys. Rev. B **92**, 245302 (2015).

[54] S.-Y. Li, Y. Su, Y.-N. Ren, and L. He, Valley polarization and inversion in strained graphene via pseudo-Landau levels, valley splitting of real Landau Levels, and confined states, Phys. Rev. Lett. **124**, 106802 (2020).

[55] S. Rachel, I. Göthel, D. P. Arovas, and M. Vojta, Strain-induced Landau levels in arbitrary dimensions with an exact spectrum, Phys. Rev. Lett. **117**, 266801 (2016).

[56] M. Settnes, S. R. Power, M. Brandbyge, and A. Jauho, Graphene nanobubbles as valley filters and beam splitters, Phys. Rev. Lett. **117**, 276801 (2016).

[57] D. Tong, Lectures on the quantum Hall effect, arXiv:1606. 06687.